Journal title

ARTICLE TYPE

Understanding of depressing surface moisture sensitivity on promoting sodium intercalation of coral-like $Na_{3.12}Fe_{2.44}(P_2O_7)_2$/C synthesized *via* a flash-combustion strategy

Bo Lin[a], Sen Zhang*[b], Chao Deng*[a]

Low-cost sodium iron pyrophosphate of $Na_{3.12}Fe_{2.44}(P_2O_7)_2$ enabling facile ion transport puts forward a promising alternative for the cathode of sodium ion batteries. However, the high moisture sensitivity and severe surface oxidation lead to its large irreversible capacity and inferior electrochemical kinetics. Herein, for the first time, we report the design of an ultrafast "flash-combustion synthesis" strategy 10 to prepare the coral-like $Na_{3.12}Fe_{2.44}(P_2O_7)_2$/C with good surface property and fast sodium intercalation. The single-phase $Na_{3.12}Fe_{2.44}(P_2O_7)_2$ is successfully prepared in as short as three minutes. Each ultrafine $Na_{3.12}Fe_{2.44}(P_2O_7)_2$ particle with a nanoscale carbon coating is enwrapped in a microscale carbon matrix, forming a coral-like architecture. Benefiting from the hierarchical carbon decoration, the coral-like composite attains good surface property that enables low moisture sensitivity and fast sodium intercalation. Moreover, the dynamic analysis reveals that surface oxidation proceeds through a "shell-core" mechanism and demonstrates the crucial 15 role of surface property on sodium intercalation. Taking advantage of the good surface property and the hierarchical porous architecture, the coral-like composite is capable of fast sodium intercalation and stable prolonged cycling. It retains 95% of the initial capacity after 200 cycles at alternative 20 and 5 *C* rates. The clarification of the correlation between the surface property and the sodium intercalation chemistry provides clues to the design and construction of high-performance $Na_{3.12}Fe_{2.44}(P_2O_7)_2$ for large-scale applications.

KEYWORDS: Flash synthesis; $Na_{3.12}Fe_{2.44}(P_2O_7)_2$; surface property; coral-like architecture; dynamic mechanism

20 1 Introduction

Realizing high-performance cathode materials is an integral aspect of the ongoing quest for building better batteries[1]. In this context, polyanion compounds with low cost and high safety are promising candidate. Since 1980s, various polyanionic materials 25 such as silicates (A_2MSiO_4)[2,3], borates $(AMBO_3)$[4], sulfates $(AMSO_4)$[5-8], phosphates $(AMPO_4)$[9-12], pyrophosphates (AMP_2O_7)[13-19], fluorophosphates $(AMPO_4F)$[20,21], and such mixed polyanions as pyrophospate-phosphates, including $(A_7M_3(P_2O_7)_4(PO_4))$[22-25], $A_4M_3(PO_4)_2(P_2O_7)$[26,27] and 30 $A_9M_3(P_2O_7)_3(PO_4)_2$[28]), and carbonate-phosphate $(A_3MCO_3PO_4)$[29,30] have been extensively studied.

Among these polyanion compounds, the pyrophosphate is an important branch, especially the multiple alkaline-ions containing pyrophosphates $(A_xM_yP_2O_7$: A=Li$^+$ and Na$^+$; M=Fe, Mn, V; 35 *x*>1)[13-19,31-36]. Since the first prediction of pyrophosphate $(Li_2MP_2O_7)$ as cathode material in 2006, a new era for the fast development of pyrophosphates is opened[31]. A series of pyrophosphates has been explored as both lithium hosts $(Li_2FeP_2O_7$[19,32], $Li_2(Fe_{1-x}Mn_x)P_2O_7$[33], $Li_2CoP_2O_7$[34]) and sodium 40 hosts $(Na_2FeP_2O_7$[13], $Na_2MnP_2O_7$[16] and $Na_{4-\alpha}M_{2+\alpha/2}(P_2O_7)_2$[15,35,36] (M=Fe, $Fe_{0.5}Mn_{0.5}$, Mn). Their open framework and facile ion

transport pathways make them promising candidate in energy storage and conversion.

45 A recently reported iron-based pyrophosphate sodium host, $Na_{3.12}Fe_{2.44}(P_2O_7)_2$, has captured our attention[15,35,36]. The symmetrically arranged FeO_6 octahedral and P_2O_7 units construct the crown unit of $Fe_2P_4O_{22}$ and $Fe_2P_4O_{20}$ for $Na_{3.12}Fe_{2.44}(P_2O_7)_2$, which results in its three-dimensional framework with reversible sodium-intercalation capability. The theoretical capacity of 50 $Na_{3.12}Fe_{2.44}(P_2O_7)_2$ based on the Fe^{2+}/Fe^{3+} redox couple reaches 117.4 mAh·g^{-1}, which makes it a competitive cathode candidate for sodium ion battery. However, suffered from the low conductivity and high surface oxidation, only *ca.* two thirds of the theoretical capacity is realized when it's first reported by Ha *et al* 55 in 2013[15]. Towards the promotion of electronic conductivity, *Niu* et al encapsulated $Na_{3.12}Fe_{2.44}(P_2O_7)_2$ in porous graphene[35] or multi-walled carbon nanotube[36]. They successfully obtained a maximum capacity close to the theoretical one, and impelled the $Na_{3.12}Fe_{2.44}(P_2O_7)_2$ to be a competitive sodium host.

60 Although remarkable improvements have been achieved, a big problem still restricts the fast development of $Na_{3.12}Fe_{2.44}(P_2O_7)_2$, that is, the high surface moisture (and CO_2) sensitivity. It induces severe surface oxidation and large initial irreversible capacity, which leads to its low electrochemical
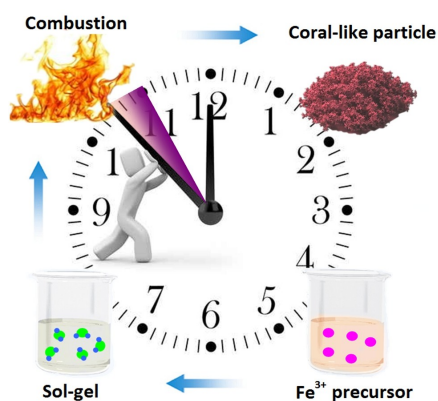
Figure 1 Schema of the flash combustion strategy for coral-like $Na_{3.12}Fe_{2.44}(P_2O_7)_2$. In the right beaker, the purple sphere represents the Fe^{3+} group. In the left beaker, the green sphere

5 represents the Fe^{2+}-based complex gel. The purple sector on the surface of watch represents the preparation time of 3 minutes.

reversibility and inferior sodium intercalation kinetics. Ha *et al* first reported the surface oxidation of air-exposed $Na_{3.12}Fe_{2.44}(P_2O_7)_2$[15]. Unfortunately, the detail of the oxidation

10 process and the dynamic mechanism are still absent until now. Therefore, it is urgent to carefully study the surface oxidation mechanism to promote the sodium intercalation into $Na_{3.12}Fe_{2.44}(P_2O_7)_2$.

On the other hand, present synthetic strategies for

15 $Na_{3.12}Fe_{2.44}(P_2O_7)_2$ are also problematic, that is, they are complicated and time/energy consuming. They usually require long-time treatment (*e.g.* 18 hours calcination)[15,34], specialized instruments (*e.g.* freeze-drying or ball milling machine)[34,35], and complicated handling[15,34,35]. These problems restrict both large-

20 scale production and commercialization of $Na_{3.12}Fe_{2.44}(P_2O_7)_2$. Therefore, it is necessary to explore a feasible synthetic strategy that is high-efficiency and easy-popularization to prepare $Na_{3.12}Fe_{2.44}(P_2O_7)_2$.

Following this viewpoint, for the first time, we use a facile

25 "flash-combustion synthesis" to prepare $Na_{3.12}Fe_{2.44}(P_2O_7)_2$/C with coral-like architecture. As illustrated in Figure 1, the synthetic route starts from a low-cost Fe(III)-based raw material. Then the Fe(II)-based precursor is achieved through a simple sol-gel process, followed by the "flash-combustion" process to obtain

30 the final product. Both the ultrafine pyrophosphate particles and the hierarchically porous frameworks are produced simultaneously within just three minutes. The whole synthetic process is easy-handling and timesaving, and moreover, the product has well-defined architecture and uniform composition.

35 As illustrated in Figure 2, the prepared $Na_{3.12}Fe_{2.44}(P_2O_7)_2$ nanoparticles are coated by nanoscale carbon layer and closely enwrapped by porous carbon matrix, which aggregates into a porous coral-like architecture. The hierarchical carbon decoration not only provides bicontinuous conductive pathways for fast

40 electron transport, but also constructs a high porous framework for high-efficiency ion transport. More importantly, the particle surface is effectively modified by dual carbon decoration, which

improves its surface physical characteristics and electrochemical kinetics.

45 To verify these advantages, the sodium intercalation chemistry and surface property of coral-like $Na_{3.12}Fe_{2.44}(P_2O_7)_2$/C are investigated. The relationships between the architecture, surface property and sodium intercalation chemistry are carefully investigated. The dynamic mechanism of surface oxidation

50 reaction is disclosed.

2 Experimental

2.1 Synthesis

Flash combustion synthesis of coral-like product

The coral-like material is prepared by a flash-combustion strategy.

55 In a typical synthesis, 6.1 mmol of iron (III) nitrate hydrate was dissolved in 40 mL distilled water to get a clear brown-yellow solution. Then 0.5 g of ascorbic acid was added to the solution and changed the color of the solution to shallow green. Next, citric acid and the mixture of 3.9 mmol sodium carbonate and 10

60 mmol ammonium dihydrogen phosphate were added to the above solution. The resultant solution was kept at 80 ^{o}C under magnetic stirring for 4 hours and dried overnight to achieve the dry gel. Finally, the precursor was grounded and subjected to calcination at 600 ^{o}C for 3 minutes under Ar atmosphere to obtain the coral-

65 like sample.

Synthesis of the reference sample

For comparison, two reference samples were prepared by solid-state strategy. Firstly, stoichiometric amount of sodium carbonate, iron(II) oxalate and diammonium hydrogen phosphate were ball-

70 milled at a rotation speed of 400 rpm. After the evaporation of solvent, the solid mixture was calcined at 300 ^{o}C for 6 hours under Ar atmosphere. Then the obtained power was grounded and re-calcined at 600 ^{o}C for 12 hours under Ar atmosphere to obtain the low-carbon reference sample. The low-carbon

75 reference sample was mixed with desirable amount of sucrose and re-calcined at 600 ^{o}C for 2 hours to obtain the carbon-coated reference sample.

2.2 Characterization

Thermogravimetric analysis (TGA, NETZSCH STA 449C) in

80 flowing nitrogen was used to monitor the combustion process of the gel precursor. Powder X-ray diffraction (XRD, Bruker D8/Germany) using Cu Kα radiation was employed to identify the crystalline phase of the material. The experiment was performed by using step mode with a fixed time of 3 s and a step

85 size of 0.02^o. Rietveld refinement was conduct using the Fullprof software. The background was refined by a Chebyshev polynomial function and the diffraction profile was fitted by a pseudo-Voigt function. The morphology was observed with a scanning electron microscope (SEM, HITACHIS-4700) and a

90 transmission electron microscope (TEM, JEOS-2010 PHILIPS). X-ray photoelectron spectroscopy (XPS, Thermo ESCALAB 250) was employed to measure the chemical state of each element in the surface. The atomic composition of prepared material was
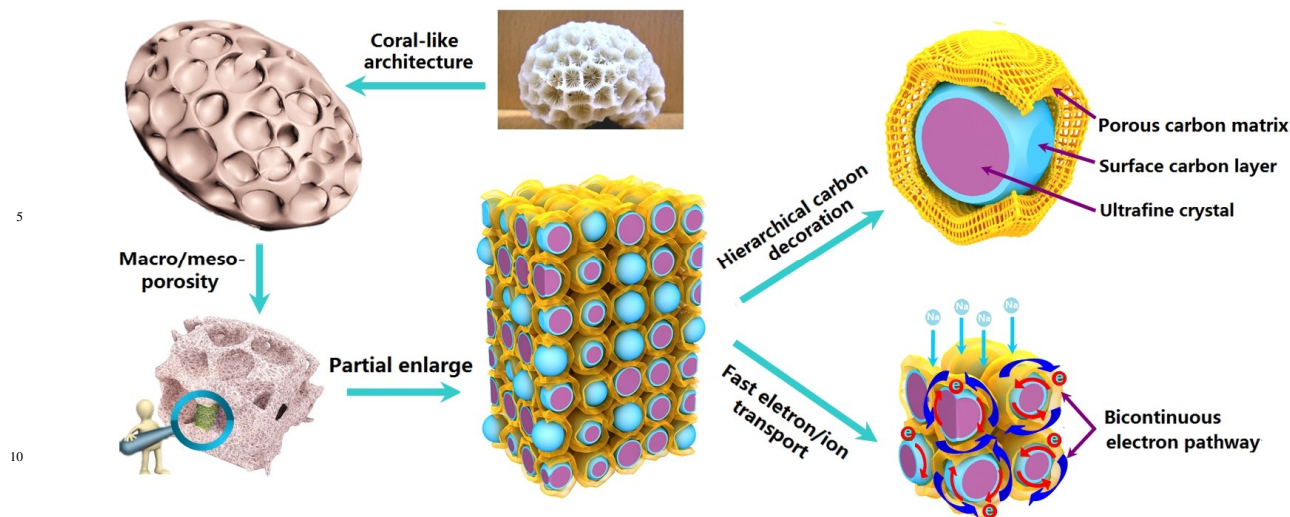
Figure 2 Schematic illustration of the architecture for the coral-like $Na_{3.12}Fe_{2.44}(P_2O_7)_2$/C composite. The partially enlarged image illustrates the hierarchical carbon decoration. The bicounitnuous electron and facile ion transport pathways are emphasized.

determined by inductively coupled plasma mass spectroscopy (ICP-MS, Agilent 7500CX). Carbon contents of the samples were determined by an element analyzer (EA, Elementar Vario EL). Raman spectra were recorded with a Labram HR-800 (HORIBA JobinYvon) spectrometer. Nitrogen adsorption-desorption isotherms were measured using a Micro-meritics ASAP 2010 sorptometer. Sample preparation included degassing at 523 K for 12 h in a vacuum of 10^{-6} Torr. Specific surface area and pore size distribution were calculated using the Brunauer-Emmett-Teller (BET) and Barrett-Joyner-Halenda (BJH) method, respectively.

2.3 Electrochemical measurements The electrochemical characteristics were measured in CR2032 coin cells. The coin cells were assembled in an argon filled glove box. Each composite electrode was made from a mixture of the active material, carbon black and polyvinylidene fluoride (PVDF) in a weight ratio of 70:15:15. The loading of the active materials in the electrodes was 3.54 mg·cm^{-2}. The thickness of the film was about 28 μm. The active mass was calculated only based on the $Na_{3.12}Fe_{2.44}(P_2O_7)_2$ without other components. Na foil was employed as counter and reference electrode and 1 mol·L^{-1} $NaClO_4$ dissolved in a mixture of ethylene carbonate and diethyl carbonate (1:1 v/v) was used as electrolyte. The galvanostatic charge/discharge cycling was tested in the voltage range of 1.6~4.0 V vs. Na$^+$/Na on a Land battery testing system (Wuhan, China). EIS measurements were conducted using a Zivelab electrochemical workstation, and the applied frequency range is 100k~0.5 mHz.

3 Results and Discussion

3.1 "flash-combustion" synthesis of coral-like architecture

First of all, the "flash-combustion" process for the preparation of coral-like $Na_{3.12}Fe_{2.44}(P_2O_7)_2$/C is monitored by thermogravimetric analysis. As displayed in Figure 3, the spectra

can be divided into four regions, *i.e.* 28~127 °C (I), 127~185 °C (II), 185~430 °C (III) and 430~800 °C (IV). In the first stage of low temperature, a weak endothermic peak with the weight loss of ~11 wt.% is observed, which is associated with the remove of residual water. Then the intense exothermic peak with sharp weight loss of ~28 wt.% is observed in stage II, indicating the drastic decomposition of the gel and simultaneous release of large amount of gases. The intense liberation of gases facilitates the formation of hierarchical pores and ultrafine particles in the final product. This phenomenon is associated with the acute redox reaction between oxidation agent (nitric anion) and reduction agent (citric acid group), which constructs the "combustion" process[19,37,38]. When the acute reaction finishes, the weight loss
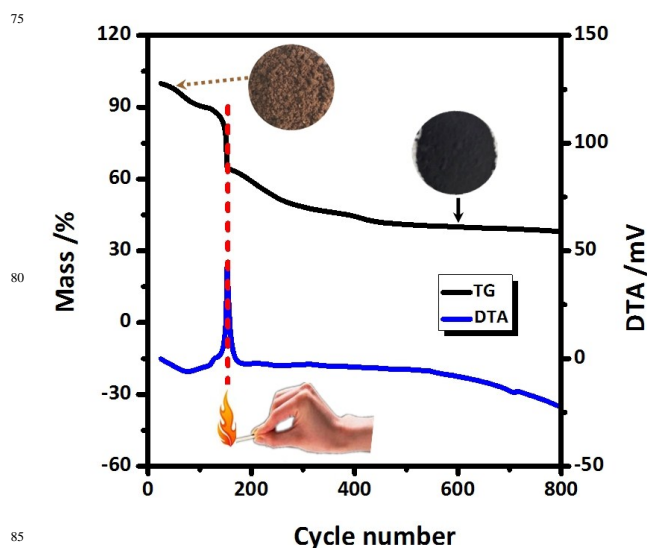

Figure 3 TG and DTA of the precursor. The photos of the precursor (brown) and target compound (black) are illustrated. The "flash-combustion" process is emphasized.
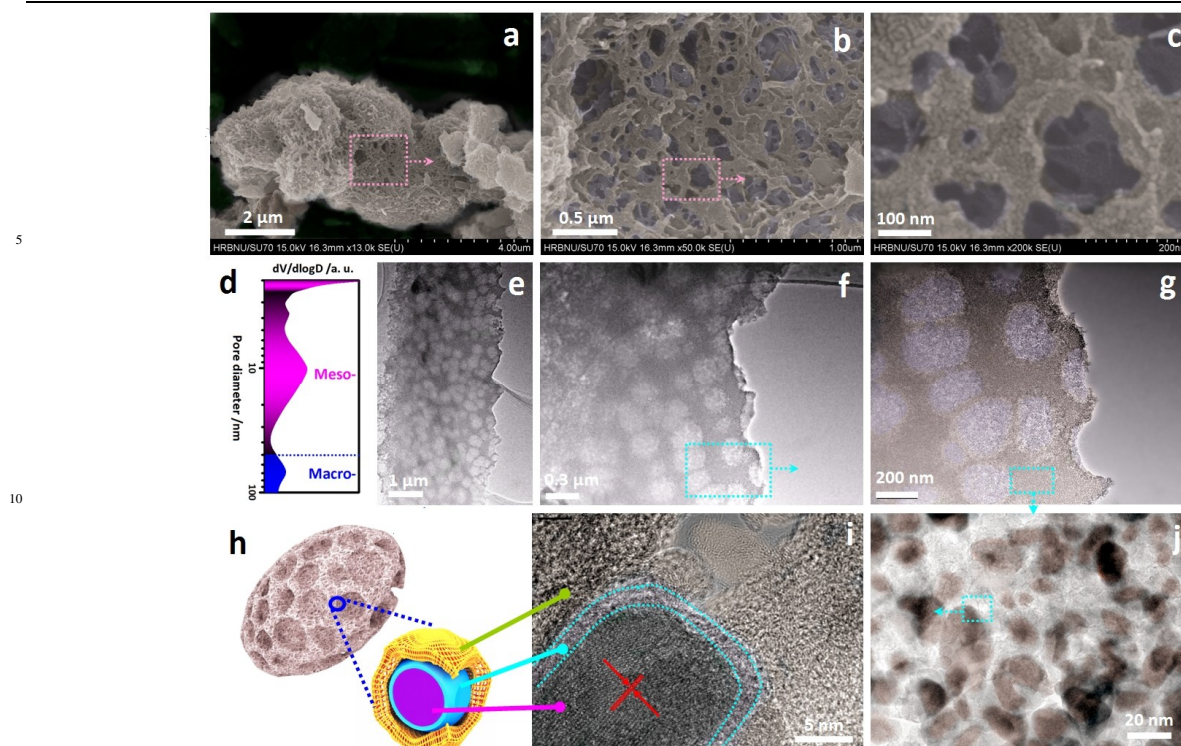
Figure 4 SEM (a~c), TEM (e~g and j) images and the pore size distribution (d) of the coral-like Na$_{3.12}$Fe$_{2.44}$(P$_2$O$_7$)$_2$/C composite. (i) HRTEM image of one nanoscale particle decorated by hierarchical carbon. (h) The schematic images of the hierarchal porous coral-like architecture (left) and one particle with dual carbon decoration (right).

turns to slow down. In stage III, the weight loss of 18 wt.% is associated with the pyrolysis of residual organic species. Finally, a minuscule exothermic peak is observed at 537 °C with insignificant weight loss (2 wt%) in stage IV, indicating the formation and perfection of the crystalline phase. The thermogravimetric results demonstrate the self-promoting characteristics of the "combustion" reaction, which supports the feasibility to reducing the reaction time. Therefore, it is favorable to employ an extreme low time of only three minutes for the ultrafast synthesis of the Na$_{3.12}$Fe$_{2.44}$(P$_2$O$_7$)$_2$ composite in our study.

The morphology and architecture of the prepared Na$_{3.12}$Fe$_{2.44}$(P$_2$O$_7$)$_2$ are investigated by SEM and TEM observations. As displayed in Figure 4 (a, e), the material exhibits a three-dimensional porous architecture on large microsize-scale. The low-resolution images (Figure 4b, f) indicate the uniformly distributed macropores with the size of 80~200 nm. The enlarged images (Figure 4c, g) demonstrate the existence of voids on the walls of macropores, which constructs the interconnections between the macropores and provides smaller mesopores. The hierarchical macro-/meso-porous architecture are further evidenced by the multiple peaks in the pore size analysis based on BJH calculation (Figure 4d). Therefore, as illustrated in Figure 4h, both the three-dimensional framework and the hierarchical porous architecture construct the coral-like structure for Na$_{3.12}$Fe$_{2.44}$(P$_2$O$_7$)$_2$. It not only facilitates easy electrolyte penetration, but also enables fast ion transport.

More details of the coral-like structure are identified by high-resolution TEM images. As displayed in Figure 4j, the framework of the coral-like structure is composed of the carbon matrix and well enwrapped nanoscale particles. The size of the particles is in the range of 10~30 nm, and its single crystal nature is evidenced by the well-resolved lattice fringe. As evidenced in Figure 4i, the interplanar distance of ~0.83 nm coincides well with the (011) lattice planes of Na$_{3.12}$Fe$_{2.44}$(P$_2$O$_7$)$_2$. Moreover, a thin carbon layer of 2~3 nm is observed on the surface of the particle, which forms a highly conductive layer surrounding the particle. As illustrated in Figure 4h, the hierarchical carbon decoration not only provides bicontinuous electron transport pathway, but also improves the surface property.

The hierarchical structure of carbon is further clarified in Figure 5. On the one hand, the surface coating layer of the particle is in the range of 2~3 nm (Figure 5b), and it is defined as the "nanoscale carbon" on particle surface. On the other hand, the carbon network surrounding the particles has plenty of pores, and it is defined as the "porous carbon" surrounding the particles (Figure 5a). As illustrated in Figure 5c, the thin surface layer corresponds to the "nanoscale carbon" (Figure 5a) and the connection part surrounding the particles corresponds to the "porous carbon" (Figure 5b). Both kinds of carbon construct the hierarchical carbon decoration for the pyrophosphate nanoparticles. Moreover, Raman spectroscopy is recorded to further characterize the nature of porous carbon in the composite. Two characteristic signature peaks located at ~1360 and 1590 cm^{-1} are observed for the composite (Figure 5d), corresponding to the
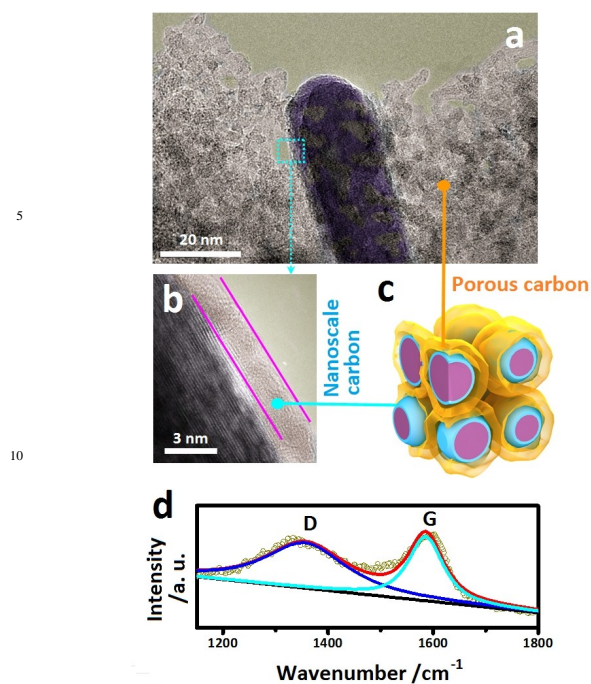
Figure 5 Hierarchical carbon decorations in the coral-like architecture. (a) Porous carbon between the $Na_{3.12}Fe_{2.44}(P_2O_7)_2$ nanoparticle. (b) Nanoscale carbon on the $Na_{3.12}Fe_{2.44}(P_2O_7)_2$ nanoparticle surface. (c) The schematic images of the hierarchical carbon decorations in coral-like architecture. (d) Raman spectroscopy of the porous carbon in the composite.

D (disordered carbon) and *G* (graphene carbon) bands. The large *D* band and the high intensity ratio of *D/G* indicate its amorphous state. Therefore, all the advantages of the coral-like structure, including dual carbon decoration, high-efficiency ion transport, bicontinous electron transport pathways and modified surface state, are beneficial to the electrochemical characteristics of $Na_{3.12}Fe_{2.44}(P_2O_7)_2$.

3.2 Moisture sensitivity and surface oxidation

In order to clarify the advantages of coral-like architecture, the surface moisture sensitivity, oxidation dynamic mechanism and sodium intercalation chemistry of the prepared sample are studied. For comparison, two reference samples, *i.e.* the low-carbon reference sample and the carbon-coated reference sample, prepared by conventional solid-state strategy are also employed in our study. The physical characteristics of the reference samples are displayed in Figure s1 and s2. The extreme low surface area of the low-carbon reference sample is associated with its large microsized particles. Although increased values have been achieved after carbon coating, the carbon-coated reference sample still exhibits much lower specific surface area than the coral-like sample. Therefore, the results demonstrate the dominant role of the hierarchical pores and ultrafine particles on the physical characteristics of the coral-like architecture.

The structures of all the samples are identified by XRD patterns. As displayed in Figure 6a, the peaks of all the samples

can be readily indexed to the triclinic structure with *P-1* space group, indicating the high purity of the prepared materials. The carbon-coated reference sample exhibits slightly weaker peaks than the low carbon reference one, but both have higher peak intensities than the coral-like one. The low crystallinity of the coral-like sample is associated with its ultrafine particles and porous structure. Rietveld refinement is carried out to more precisely evaluate the $Na_{3.12}Fe_{2.44}(P_2O_7)_2$ phase. As displayed in Figure 6b, the well matched patterns certify the good reliability of the calculations. The obtained lattice parameters of all the samples are listed in table s1, which coincided well with previous reports[15,35,36]. The crystal structure of the $Na_{3.12}Fe_{2.44}(P_2O_7)_2$ phase is illustrated in Figure 6c. Two FeO_6 octahedra and two P_2O_7 group construct the crown unit of $Fe_2P_4O_{22}$ and $Fe_2P_4O_{20}$, which constructs the basic unit of $Na_{3.12}Fe_{2.44}(P_2O_7)_2$ through corner sharing. The 3D framework of $Na_{3.12}Fe_{2.44}(P_2O_7)_2$ not only provides interstitial spaces for sodium accommodation, but also offers channel for ion transport. Moreover, the elemental analysis results (Table s2) demonstrate the coincidence of the atomic ratios between the prepared materials and the designed value.

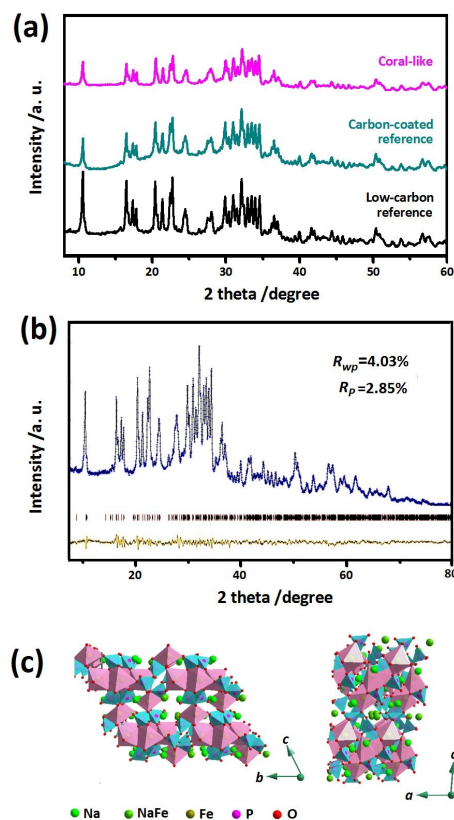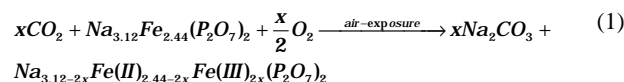
Figure 6 (a) XRD patterns of the coral-like sample, carbon-coated reference and low-carbon reference sample. (b) Rietveld refinement of the coral-like sample. (c) Crystal structure of the triclinic $Na_{3.12}Fe_{2.44}(P_2O_7)_2$. The experimental data (blue dot), calculated pattern (black line), their difference (yellow line) and the Bragg diffraction positions (pink ticks) are displayed in b.

Therefore, both the structure and composition analysis results demonstrate that the target product of $Na_{3.12}Fe_{2.44}(P_2O_7)_2$ has been successfully prepared.

The high moisture/CO_2 sensitivity is a major defect of $Na_{3.12}Fe_{2.44}(P_2O_7)_2$, which leads to severe surface oxidation and deteriorated electrochemical property. In order to investigate the effects of the coral-like architecture on the moisture sensitivity of $Na_{3.12}Fe_{2.44}(P_2O_7)_2$, we investigate the surface states of all the samples by XPS measurements. As displayed in Figure 7a, two peaks are observed in the C1s spectra for the low-carbon reference sample. The major peak at lower binding energy (284.6 eV) originates from the residual carbon on the $Na_{3.12}Fe_{2.44}(P_2O_7)_2$ particles. The minor peak at higher binding energy (288.5 eV) originates from Na_2CO_3, which is the product of the surface oxidation reaction as described in the following equation.

$$xCO_2 + Na_{3.12}Fe_{2.44}(P_2O_7)_2 + \frac{x}{2}O_2 \xrightarrow{air-exposure} xNa_2CO_3 + \tag{1}$$
$$Na_{3.12-2x}Fe(II)_{2.44-2x}Fe(III)_{2x}(P_2O_7)_2$$

Similar phenomenon has also been observed by Ha *et al* [15], who had verified the high moisture sensitivity and surface oxidation of $Na_{3.12}Fe_{2.44}(P_2O_7)_2$. The carbon-coated reference sample exhibits much lower high-binding-energy peak than the low-carbon reference one, indicating the quantities of Na_2CO_3 decreases after surface encapsulation (Figure 7b). Moreover, almost no high-binding-energy peak is observed for the coral-like sample, certifying the extreme low Na_2CO_3 content on its surface (Figure 7c).

Similarly, both O1s (Figure 7d) and Na1s (Figure 7g) spectra of the low-carbon reference sample also exhibit two distinct peaks, *i.e.* the major peak at low binding energy and the minor peak at high binding energy. It indicates the existence of both $Na_{3.12}Fe_{2.44}(P_2O_7)_2$ and Na_2CO_3 on particle surface. After surface encapsulation, the high-binding-energy peaks in Na1s and O1s spectra decrease (Figure 7e and h), certifying the decreased Na_2CO_3 content for the carbon-coated reference sample. Moreover, almost no high-binding-energy peaks are observed on the Na1s and O1s spectra for the coral-like sample (Figure 7f and i), indicating the extremely low Na_2CO_3 content on its surface.

Therefore, the XPS results demonstrated that the surface encapsulation is beneficial to depress the surface oxidation of $Na_{3.12}Fe_{2.44}(P_2O_7)_2$. Moreover, the highest surface purity of the coral-like sample further verifies the high-efficiency of coral-like architecture on the inhibition of surface oxidation reaction. It is associated with the hierarchical carbon decoration and uniform ultrafine particles, which modifies the surface property and effectively suppress its moisture/CO_2 sensitivity.

3.3 Dynamic oxidation mechanism

In order to clarify the mechanism of coral-like architecture on the depression of moisture sensitivity, dynamic studies are carried out. We exposed all of the samples to ambient environment for different time. Figure 8a~c illustrates the Nyquist plots of all the samples with different air-exposure time. The spectra consist of the arc in the high frequency and the
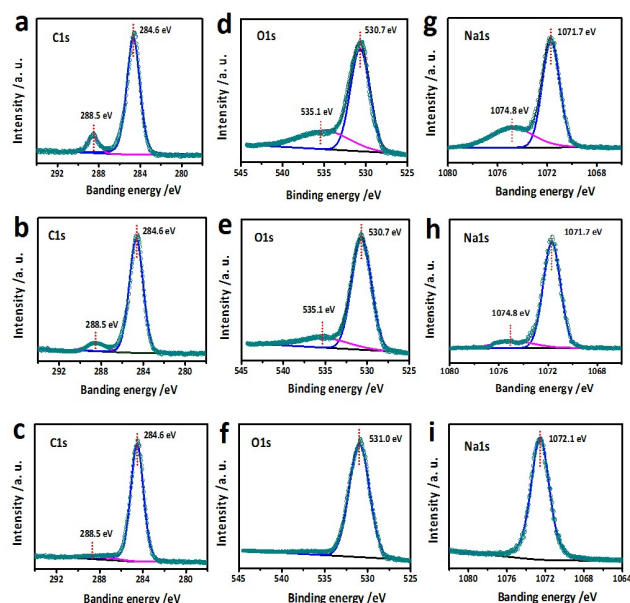

Figure 7 C1s (a~c), O1s (d~f) and Na1s (g~i) of the low-carbon reference (a, d, g), carbon-coated reference (b, e, h) and coral-like (c, f, i) samples.

inclined line in the low frequency. The high frequency part is attributed to the charge (electron) injection across the interface of the electrode material; and the low frequency part corresponds to the solid-state diffusion of sodium ions[39,40]. Therefore, the electrochemical resistance (R) corresponding to the high-frequency arc is employed to monitor the effect of air-exposure.

As displayed in Figure 8d, when the exposure time is increased, the R values of all the samples initially jump up, and then slowly increase and finally become stable. The coral-like sample exhibits much lower R values than the reference ones, suggesting its better charge (electron) transfer capability. The change fashion of R values with altering the exposure time demonstrates the oxidation process is not uniform in the whole time range. Therefore, an apparent oxidation rate is calculated to further characterize the oxidation reaction based on the following equation:

$$v = \Delta R / \Delta t \tag{2}$$

where v is the apparent oxidation rate; R is the electrochemical resistance; t is the air exposure time.

Figure 8e displays the relationship between the apparent oxidation rate and the air-exposure time. For all the samples, when the exposure time is increased, apparent oxidation rates initially jump up, and then turn to slow increase and finally become stable. The carbon-coated reference sample exhibits lower oxidation rate than the low-carbon reference one. Both reference samples exhibit higher oxidation rates than the coral-like one. Therefore, the results demonstrate that the coral-like architecture facilitates the suppression of the oxidation rate and promotes the electrochemical kinetics. Moreover, the slowing of the oxidation rate with increasing exposure time also indicates
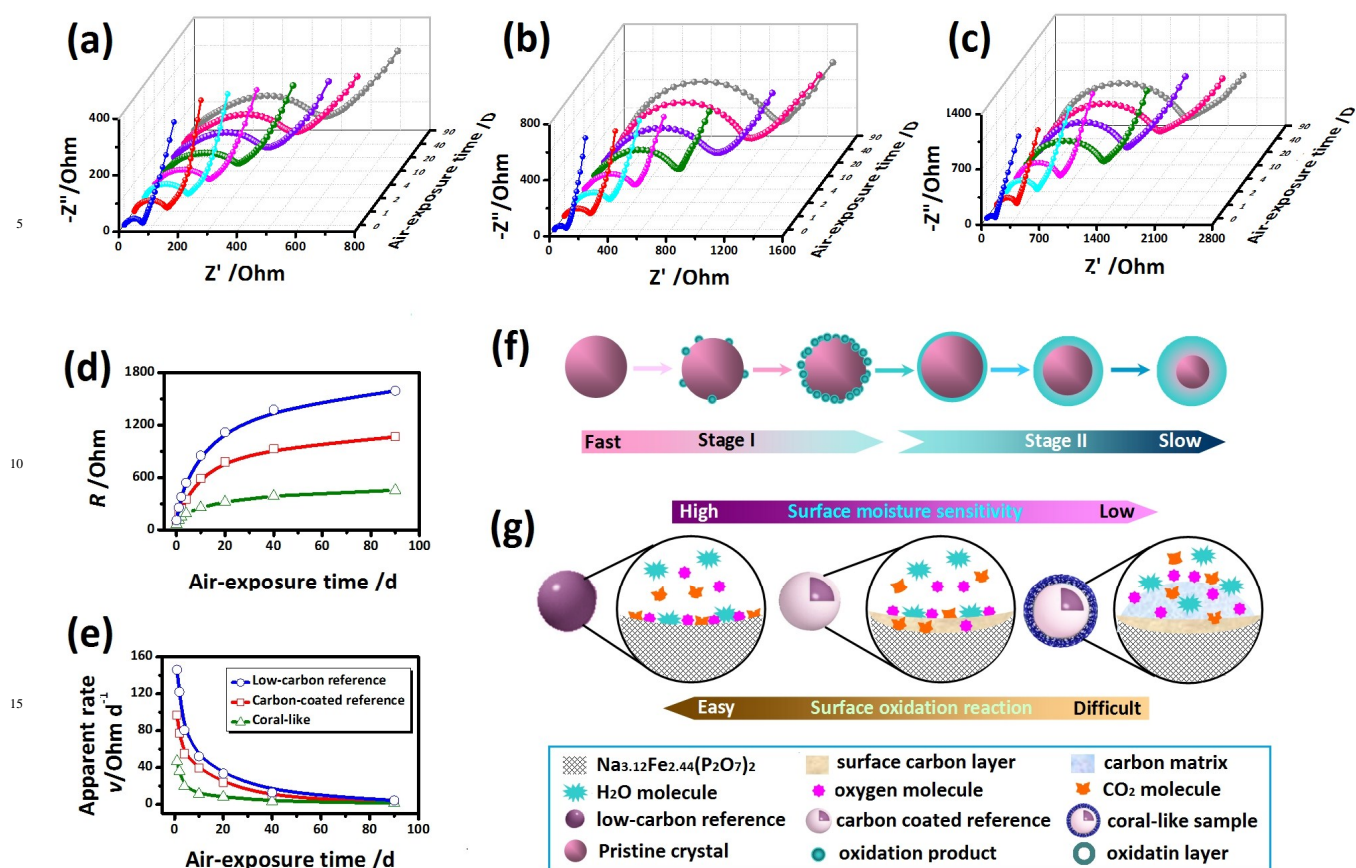
Figure 8 Nyquist plots of the coral-like sample (a), carbon-coated reference (b) and low-carbon reference (c) with different air-exposure time. The relationships between the electrochemical resistance (d) and calculated apparent oxidation rate (e) to the air-exposure time. (f) "shell-core" model of $Na_{3.12}Fe_{2.44}(P_2O_7)_2$ during air-exposure. (g) Schematic illustration of the surface oxidation reaction for the low-carbon reference, carbon-coated reference and coral-like samples during air exposure.

that the prior formed oxidation product will arrest the following oxidation reaction on the particle.

Based on above result, it is deduced that the oxidation reaction asymmetrically takes place from surface to the inside of the particle. Therefore, a "shell-core" model is set up to characterize the oxidation process of $Na_{3.12}Fe_{2.44}(P_2O_7)_2$ particle. As schematically illustrated in Figure 8f, the entire oxidation process can be divided into two stages, that is, stage I with faster oxidation rate and stage II with slower rate. At stage I, the oxidation reaction starts from some certain points, which results in oxidation product scattered on the particle surface. Then the oxidized surface continuously increases as the oxidation reaction proceeds. The oxidation rate of this stage is proportional to the area of the virgin surface. At this stage, the oxidation reaction is easy to take place and the oxidation rate is fast.

When the entire particle surface is oxidized, it comes to the stage II. At this stage, the integrated oxidation layer is formed and covers the particle surface. The oxidation reaction has to penetrate through the outer "oxidation shell" to reach the inner part of the particle, which seriously restricts the oxidation rate. As exposure time increases, the thickness of oxidation shell increases. It is even harder for the oxidation reaction to take place in the

"inner" part of the particle, which leads to the lower oxidation rate. The oxidation rate of this stage is inversely proportional to the thickness of the "shell". At this stage, the oxidation reaction is difficult to take place and the oxidation rate finally stabilizes at an extreme low value near zero. The "shell-core" model coincides well with the above experimental results. Therefore, it is proposed as a valid mechanism to explain the oxidation process for $Na_{3.12}Fe_{2.44}(P_2O_7)_2$.

Based on the "shell-core" mechanism, the role of surface encapsulation on the moisture sensitivity and surface oxidation is disclosed. As illustrated in Figure 8g, the oxidation reaction can easily take place on the particle surface of the low-carbon reference sample, because it has large pristine area under air-exposure. After surface encapsulation, a protective layer is produced for the carbon-coated reference sample. It effectively decreases the contact between the particle surface and the moisture, oxygen and CO_2. Thus the surface oxidation reaction is suppressed and the oxidation rate is decreased. Furthermore, the coral-like architecture provides dual-protection for $Na_{3.12}Fe_{2.44}(P_2O_7)_2$ crystal by hierarchical carbon decoration. It remarkably restricts the oxidation reaction and results in the extreme low oxidation rates. Therefore, it facilitates the

depressing of the moisture sensitivity and prevents the oxidation reaction on particle surface. Taking the advantages of promoted surface property, bicontinous electron transport pathways and easy electrolyte penetration, the coral-like architecture shows absolute superiority on both the electrochemical reversibility and sodium intercalation kinetics for $Na_{3.12}Fe_{2.44}(P_2O_7)_2$.

3.4 Sodium intercalation chemistry

The sodium intercalation characteristics of the $Na_{3.12}Fe_{2.44}(P_2O_7)_2$ composites were investigated. First of all, the galvanostatic charge-discharge curves in initial two cycles are displayed in figure 9 (a, c, e). The low-carbon reference sample exhibits a high initial charge capacity of 167 mAh g^{-1}, but only 84 mAh g^{-1} of the capacity is reversibly achieved in the following discharge. Almost half of the invalid irreversible capacity evidenced its poor electrochemical reversibility. Compared with the low-carbon reference sample, the carbon-coated reference sample exhibits lower initial charge capacity and higher initial discharge capacity, resulting in decreased irreversible capacity.
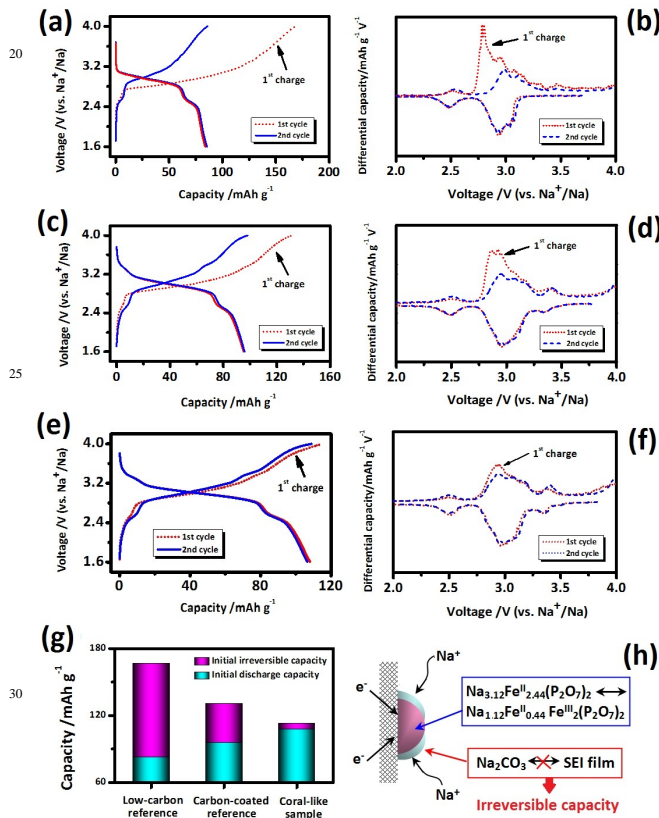

Figure 9 Galvanostatic charge/discharge curves (a, c, e) and calculated differential capacities (b, d, f) of the low-carbon reference (a, b), carbon-coated reference (c, d) and coral-like (e, f) samples during initial two cycles. (g) Comparison of their irreversible capacities and discharge capacities in the first cycle. (h) Schematic illustration of the reactions taken place on the solid/electrolyte interface of a partial oxidized $Na_{3.12}Fe_{2.44}(P_2O_7)_2$ particle. The pink semicircle represents $Na_{3.12}Fe_{2.44}(P_2O_7)_2$ and the blue part represents the oxidation product on particle surface.

For the coral-like sample, the difference between the initial charge and discharge capacities is negligible, certifying its lowest irreversible capacity among the samples (Figure 9g).

Electrochemical voltage spectroscopy (EVS) analysis was also conducted to clarify the advantages of surface encapsulation. The redox peaks in the differential capacity curve correspond to the charge/discharge plateaus in the galvanostatic charge/discharge curves. As displayed in Figure 9 (b, d and f), all of the samples have three pairs of redox peaks in the differential capacity curves, which corresponds to a sequence of sodium intercalation steps based on the Fe^{2+}/Fe^{3+} redox reaction of $Na_{3.12}Fe_{2.44}(P_2O_7)_2$[15]. The potential difference between the redox peaks in the EVS curves is used to differentiate the electrochemical reversible of electrode materials. A lower potential difference is an indication of a higher electrochemical reversibility[40,41]. Compared with the low-carbon reference sample, the carbon-coated and coral-like samples exhibit lower potential difference, indicating their higher electrochemical reversibility. Moreover, the coral-like sample exhibits the lowest difference between the first and second charge among all the samples, demonstrating its best electrochemical reversibility.

The different electrochemical reversibility is associated with the different surface property of the samples. As illustrated in Figure 9h, when the partly oxidized $Na_{3.12}Fe_{2.44}(P_2O_7)_2$ particle is employed as a cathode material in sodium ion battery, two kinds of reactions will take place simultaneously on the solid/electrolyte interface. One is the Fe^{2+}/Fe^{3+} redox reaction of $Na_{3.12}Fe_{2.44}(P_2O_7)_2$ phase. It accompanies the reversible sodium intercalation/deintercalation and provides effective capacity for the $Na_{3.12}Fe_{2.44}(P_2O_7)_2$ electrode. The other is the reaction between the electrolyte and the oxidized product of sodium carbonate, which leads to invalid irreversible capacity and forms the SEI film covering on the particle surface. It severely deteriorates the electrochemical reversibility and restricts the electrochemical kinetics. Therefore, the moisture sensitivity and surface property are critical to determine the sodium intercalation capability of $Na_{3.12}Fe_{2.44}(P_2O_7)_2$.

As discussed above, the low-carbon reference sample with high moisture sensitivity possesses large amount of oxidation product on its particle surface. The reaction of these oxidation products with electrolyte leads to its high irreversible capacity, low discharge capacity and poor sodium intercalation kinetics. When the surface is modified by carbon coating, the moisture sensitivity of the modified sample is depressed and the electrochemical reversibility is improved correspondingly. As to the coral-like sample, double-protections are constructed and a "clean" surface is obtained. It is favorable to both electrochemical reversibility and sodium intercalation kinetics for the coral-like $Na_{3.12}Fe_{2.44}(P_2O_7)_2$.

Encouraged by the advantages of coral-like architecture, its high rate capability and cycling stability are investigated. A series of current densities, from 0.05 C to 20 C, are employed to evaluate the rate capability. As compared in Figure 10b, the coral-like sample obviously exhibits higher capacity than the
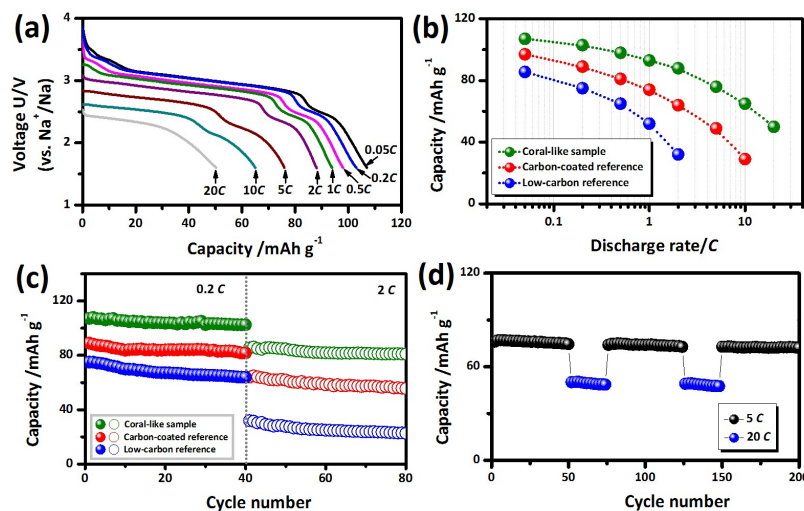
Figure 10 Rate capability and cycling property: (a) Galvanostatic discharge curves of the coral-like sample at different rates. Comparisons of the rate capacities (b) and cycling property (c) between the coral-like, carbon-coated reference and low-carbon reference samples. (d) Long-term cycling property of the coral-like sample at alternative 5 C and 20 C.

reference samples at all current densities. As the current density increases, the capacity difference between the samples becomes more significant. For example, the coral-like composite delivers 107 and 88 mAh·g^{-1} at the 0.05 C and 2 C rates, but only 97 and 86 mAh·g^{-1} (0.05 C) and 64 and 32 mAh·g^{-1} (2 C) are obtained for the carbon-coated and low-carbon reference samples, respectively. The cycling performances of all samples are investigated at both low (0.2 C) and high (2 C) rates. As compared in Figure 10c, the coral-like sample achieves the capacity retentions of 96.0% and 95.3% at 0.2 C and 2 C, which are higher than those of the carbon-coated reference (92.1% at 0.2 C and 88.3% at 2 C) and the low-carbon reference (86.9% at 0.2 C and 72% at 2 C) samples. Moreover, the coral-like sample also achieves excellent long-term cycling property, which retains 95% of the initial capacity after 200 cycles at alternate 20 C and 5 C (Figure 10d).

The above results demonstrate the superior high rate capability and excellent cycling stability of the coral-like sample. It can be attributed to two factors. On the one hand, the modified surface facilitates the improvement of electrochemical reversibility and sodium intercalation kinetics. It effectively depresses the side reaction of electrolyte decomposition and enables high-efficiency sodium intercalation. On the other hand, the high porosity and high conductive framework are favorable to electron/ion transport, which facilitates fast sodium intercalation. Moreover, the hierarchical porous architecture also acts as a buffer layer for $Na_{3.12}Fe_{2.44}(P_2O_7)_2$ crystal during sodium de/intercalation, which promotes its long-term cycling stability. Therefore, the coral-like architecture is a good model to modify the surface property and realize superior electrochemical characteristics for $Na_{3.12}Fe_{2.44}(P_2O_7)_2$.

4 Conclusions

Aiming at depressing the moisture sensitivity and promoting the sodium intercalation capability, we designed an ultrafast "flash-combustion" approach to prepare $Na_{3.12}Fe_{2.44}(P_2O_7)_2$ in coral-like architecture. The ultrafine $Na_{3.12}Fe_{2.44}(P_2O_7)_2$ nanoparticles and porous carbon framework are simultaneously synthesized within just three minutes. Taking the advantage of "dual-protection" from hierarchical carbon decoration, the coral-like composite achieves a "clean" surface with depressed moisture sensitivity and improved electrochemical reversibility. In order to clarify the effects of surface encapsulation, the dynamic mechanism of surface oxidation reaction is carefully studied, and moreover, a shell-core model is set up. Benefiting from the promoted surface property and the hierarchical porous architecture, the composite achieves superior electron/ion transport capability and excellent long-term cycling stability. The deep insight into the correlation between surface property and sodium intercalation chemistry in this study provides clues to the rational design and construction of high-performance $Na_{3.12}Fe_{2.44}(P_2O_7)_2$ for commercial production.

Acknowledgement

Notes and references

[a]Key Laboratory for Photonic and Electronic Bandgap Materials, Ministry of Education; College of Chemistry and Chemical Engineering, Harbin Normal University, Harbin, 150025, Heilongjiang, China; E-Mail: chaodenghsd@sina.com
[b]Key Laboratory of Superlight Material and Surface Technology, Ministry of Education, College of Material Science and Chemical Engineering,

Harbin Engineering University, Harbin 150001, Heilongjiang, China; E-Mail: senzhang@hrbeu.edu.cn

1   N. Yabuuchi, K. Kubota, M. Dahbi, S. Komaba, *Chem. Rev.* **2014**, *114*, 11636-11682.

2   C. Deng, S. Zhang, S. Y. Yang, *Mater. Chem. Phys.* **2010**, *120*, 14-17.

3   S. Zhang, C. Deng, H. Gao, F. L. Meng, M. Zhang, *Electrochim. Acta* **2013**, *107*, 406-412.

4   L. Tao, G. Rousse, J. N. Chotard, L. Dupont, S. Bruyere, D. Hanzel, G. Mali, R. Dominko, S. Levasseur, C. Masquelier, *J. Mater. Chem. A* **2014**, *2*, 2060-2070.

5   P. Barpanda, G. Oyama, C. D. Ling, A. Yamada, *Chem. Mater.* **2014**, *26*, 1297-1299.

6   P. Barpanda, G. Oyama, S. I. Nishimura, S. C. Chung, A. Yamada, *Nat. Commu.* **2014**, *5*, 4358.

7   Y. Meng, S. Zhang, C. Deng, *J. Mater. Chem. A* **2015**, *3*, 4484-4492.

8   Y. Meng, T. T. Yu, S. Zhang, C. Deng, *J. Mater. Chem. A* **2015**, DOI:10.1039/C5ta07696j.

9   A. K. Padhi, K. S. Nanjundaswamy, J. B. Goodenough, *J. Electrochem. Soc.* **1997**, *144*, 1188-1194.

10   P. Moreau, D. Guyomard, J. Gaubicher, F. Boucher, *Chem. Mater.* **2010**, *22*, 4126-4128.

11   Q. Y. Wang, B. D. Zhao, S. Zhang, X. H. Gao, C. Deng, *J. Mater. Chem. A* **2015**, *3*, 7732-7740.

12   S. Y. Yang, S. Zhang, B. L. Fu, Q. Wu, F. L. Liu, C. Deng, *J. Solid State Electrochem.* **2011**, *15*, 2633-2638.

13   P. Barpanda, G. D. Liu, C. D. Ling, M. Tamaru, M. Avdeev, S. C. Chung, Y. Yamada, A. Yamada, *Chem. Mater.* **2013**, *25*, 3480-3487.

14   P. Barpanda, S. Nishimura, A. Yamada, *Adv. Energy Mater.* **2012**, *2*, 841-859.

15   K. H. Ha, S. H. Woo, D. G. Mok, N. S. Choi, Y. Park, S. M. Oh, Y. Kim, J. Kim, J. Lee, L. F. Nazar, K. T. Lee. *Adv. Energ. Mater.* **2013**, *3*, 770-776.

16   P. Barpanda, T. Ye, M. Avdeev, S. C. Chung, A. Yamada, *J. Mater. Chem. A,* **2013**, *1*, 4194-4197.

17   H. Kim, R. A. Shakoor, C. Park, S. Y. Lim, J. S. Kim, Y. N. Jo, W. Cho, K. Miyasaka, R. Kahraman, Y. Jung, J. W. Choi, *Adv. Funct. Mater.* **2013**, *23*, 1147-1155.

18   P. Barpanda, J. Lu, T. Ye, M. Kajiyama, S. C. Chung, *RSC Adv.*, **2013**, *3*, 3857-3860.

19   L. Tan, S. Zhang, C. Deng, *J. Power Sources* **2015**, *275*, 6-13.

20   Z. Liu, Y. Y. Hu, M. T. Dunstan, H. Huo, X. G. Hao, H. Zou, G. M. Zhong, Y. Yang, C. P. Grey, *Chem. Mater.* **2014**, *26*, 2513-2521.

21   W. X. Song, X. B. Ji, Z. P. Wu, Y. C. Yang, Z. Zhou, F. Q. Li, Q. Y. Chen, C. E. Banks, *J. Power Sources*, **2014**, *256*, 258-263.

22   S. Y. Lim, H. Kim, J. Chung, J. H. Lee, B. G. Kim, J. J. Choi, K. Y. Chung, W. Cho, S. J. Kim, W. A. Goddard, Y. S. Jung, J. W. Choi. *PNAS* **2014**, *111*, 599-604.

23   C. Deng, S. Zhang. *ACS Appl. Mater. Interfaces* **2014**, 6, 9111-9117.

24   S. Zhang, C. Deng, Y. Meng, *J. Mater. Chem. A* **2014**, *2*, 20538-20544.

25   C. Deng, S. Zhang, Y. X. Wu, *Nanoscale* **2015**, *7*, 487-491.

26   H. Kim, I. Park, D. H. Seo, S. Lee, S. W. Kim, W. J. Kwon, Y. U. Park, C. S. Kim, S. Jeon, K. Kang, *J. Am. Chem. Soc*. **2012**, *134*, 10369-10372.

27   H. Kim, I. Park, S. Lee, H. Kim, K. Y. Park, Y. U. Park, H. Kim, J. Kim, H. D. Lim, W. S. Yoon, K. Kang, *Chem. Mater.* **2013**, *25*, 3614-3622.

28   H. Gao, S. Zhang, C. Deng, *Dalton Trans.* **2015**, *44*, 138-145.

29   H. L. Chen, G. Hautier, G. Ceder, *J. Am. Chem. Soc.* **2012**, *134*, 19619-19627.

30   H. L. Chen, G. Hautier, A. Jain, C. Moore, B. Kang, R. Doe, L. J. Wu, Y. Z. Zhu, G. Ceder, *Chem. Mater.* **2012**, *24*, 2009-2016.

31   J. Barker, M. Y. Saidi, U.S. Patent 7008566, 2006.

32   S. Nishimura, M. Nakamura, R. Natsui, A. Yamada, *J. Am. Chem. Soc.* **2010**, *132*, 13596-13597

33   N. Furuta, S. Nishimura, P. Barpanda, A. Yamada, *Chem. Mater.* **2012**, *24*, 1055-1061.

34   S. Lee, S. S. Park, *Chem. Mater.* **2012**, *24*, 3550-3557.

35   Y. Niu, M. Xu, S. Bao, C. Li, *Chem. Commun.* 2015, DOI: 10.1039/C5CC04422G.

36   Y. B. Niu, M. W. Xu, C. J. Cheng, S. J. Bao, J. K. Hou, S. G. Liu, F. L. Yi, H. He, C. M. Li, *J. Mater. Chem. A* **2015**, 3, 17224-17229.

37   T. V. Anuradha, S. Ranganathan, T. Mimani, K. C. Patil, *Scripta Mater.* **2001**, *44*, 2237-2241.

38   M. R. Barati, *J. Sol-gel Sci. Technol.* **2009**, *52*, 171-178.

39   C. Deng, S. Zhang, B. L. Fu, S. Y. Yang, L. Ma, *J. Alloys Compd.* **2010**, *496*, 521-527.

40   C. Deng, S. Zhang, S. Y. Yang, B. L. Fu, L. Ma, *J. Power Sources* **2011**, *196*, 386-392.

41   S. Zhang, C. Deng, S. Y. Yang, L. Ma, *J. Alloys Compd.* **2009**, *484*, 519-523.

Graphic Abstract
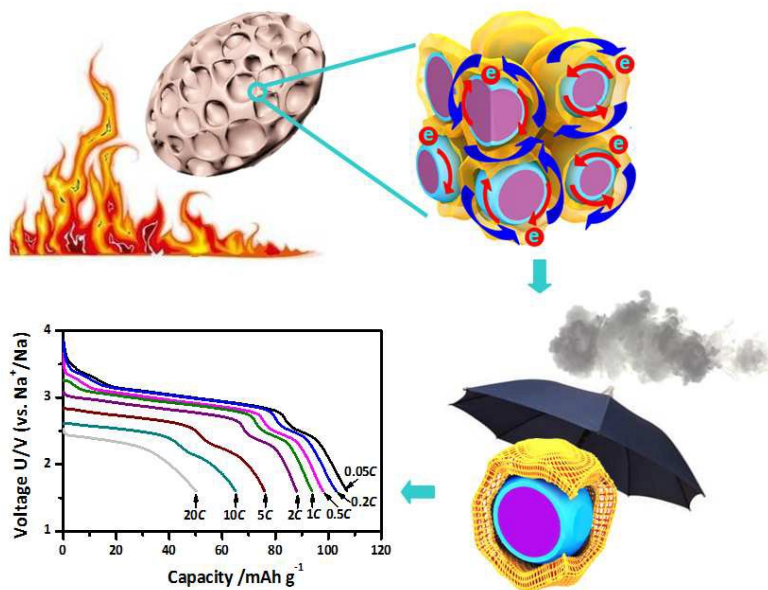
The flash-combustion synthesis provides a high-efficiency strategy for the preparation of coral-like $Na_{3.12}Fe_{2.44}(P_2O_7)_2$ with good surface property and fast sodium intercalation.